

Water-mass transformation by sea ice in the upper branch of the Southern Ocean overturning

Ryan P. Abernathey^{1*}, Ivana Cerovecki², Paul R. Holland³, Emily Newsom⁴, Matt Mazloff² and Lynne D. Talley²

Ocean overturning circulation requires a continuous thermodynamic transformation of the buoyancy of seawater. The steeply sloping isopycnals of the Southern Ocean provide a pathway for Circumpolar Deep Water to upwell from mid depth without strong diapycnal mixing^{1–3}, where it is transformed directly by surface fluxes of heat and freshwater and splits into an upper and lower branch^{4–6}. While brine rejection from sea ice is thought to contribute to the lower branch⁷, the role of sea ice in the upper branch is less well understood, partly due to a paucity of observations of sea-ice thickness and transport^{8,9}. Here we quantify the sea-ice freshwater flux using the Southern Ocean State Estimate, a state-of-the-art data assimilation that incorporates millions of ocean and ice observations. We then use the water-mass transformation framework¹⁰ to compare the relative roles of atmospheric, sea-ice, and glacial freshwater fluxes, heat fluxes, and upper-ocean mixing in transforming buoyancy within the upper branch. We find that sea ice is a dominant term, with differential brine rejection and ice melt transforming upwelled Circumpolar Deep Water at a rate of $\sim 22 \times 10^6 \text{ m}^3 \text{ s}^{-1}$. These results imply a prominent role for Antarctic sea ice in the upper branch and suggest that residual overturning and wind-driven sea-ice transport are tightly coupled.

The Southern Ocean State Estimate (SOSE) is an ice/ocean data assimilation produced for the time period January 2005 through December 2010. (See Methods and Supplementary Information for SOSE details and validation.) The bulk freshwater fluxes at the ocean surface south of 50° S, as estimated by SOSE, are summarized in Fig. 1a. When sea ice forms, nearly all of the salt remains behind in the underlying seawater (a process called brine rejection); when the ice melts, liquid freshwater is returned to the ocean. Direct open-ocean precipitation minus evaporation (0.28 fwSv) and glacial ice melt (0.05 fwSv) are both smaller than net sea-ice melt (0.50 fwSv) and brine rejection (0.36 fwSv). (Bulk freshwater volume fluxes are given in units of freshwater sverdrups¹¹, 1 fwSv = $10^6 \text{ m}^3 \text{ freshwater s}^{-1} \simeq 3.15 \times 10^4 \text{ Gt freshwater per year}$.) Melt exceeds brine rejection because sea ice incorporates snowfall at a rate of 0.14 fwSv. Moreover, wind-driven sea-ice transport creates a freshwater conveyor belt from the Antarctic coast to the open ocean¹², leading to sharp gradients in freshwater flux. The spatial structure of the sea-ice redistribution is assessed in Fig. 1b by comparing the annual mean freshwater flux leaving the atmosphere, land and glaciers (left panel) with that entering the ocean (right panel); the difference is due to sea-ice freshwater redistribution (middle panel, vectors show the ice thickness transport). From

the atmosphere, widespread precipitation over the Southern Ocean leads to a broadly distributed downward freshwater flux with a characteristic magnitude of 0.5 m yr^{-1} , and glacial ice melt provides a stronger freshwater source near the Antarctic coast. (SOSE does not include subsurface ice-shelf fluxes.) Sea ice reverses the sign of the freshwater flux near the coast, through both brine rejection and snow interception. Ice is blown away from Antarctica by winds and melts near the Southern Front of the Antarctic Circumpolar Current, where the melt flux exceeds the precipitation rate. The large sea-ice freshwater fluxes have a major impact on the density of seawater, and consequently, the stratification and circulation of the Southern Ocean.

The importance of brine rejection for the production of high-salinity shelf water (HSSW), and eventually Antarctic Bottom Water (AABW), is broadly accepted, although the magnitude of the production rate is highly uncertain⁷. Modelling studies have shown a relationship between lateral transport of Antarctic sea ice and the strength of the AABW cell^{13–15}. Model experiments have also shown that the excess freshwater exported via sea ice to the open Southern Ocean contributes to the production of fresh Antarctic Intermediate Water (AAIW), suggesting that sea ice helps sustain the upper branch of the overturning¹⁶. It has further been argued that the buoyancy gain in upwelling Circumpolar Deep Water (CDW) comes primarily from freshwater fluxes, not heat fluxes¹⁷.

To quantify the role of sea-ice processes on the overturning circulation, we apply the water-mass transformation framework¹⁰, which quantifies the rate at which a given water mass is made lighter (negative transformation rate) or denser (positive) due to diabatic processes, that is, surface fluxes and mixing. (See Methods and Supplementary Information for details of the calculation.) Integrated over a basin, the transformation rate represents the net volume flux across an isopycnal surface. If this volume flux is not constant in the upper ocean over a given density range, it implies that water must be subducted to or upwelled from the interior in that range order to satisfy mass continuity¹⁸, providing a quantitative link between surface thermodynamic processes and overturning circulation. A few past studies have calculated the transformation rate due to ocean–ice freshwater exchange as part of more general analyses of model simulations^{17,19}. Here we apply this approach within the SOSE framework of assimilated observations, thereby making dynamically consistent use of all the streams of observational data. By separately diagnosing the density transformation driven by sea-ice, atmospheric and glacial freshwater exchange, as well as by heat fluxes and upper-ocean mixing, we quantify the importance of each process in

¹Lamont Doherty Earth Observatory of Columbia University, Palisades, New York 10964, USA. ²Scripps Institution of Oceanography, La Jolla, California 92093, USA. ³British Antarctic Survey, Cambridge CB3 0ET, UK. ⁴University of Washington, Seattle, Washington 98195, USA.

*e-mail: rpa@ldeo.columbia.edu

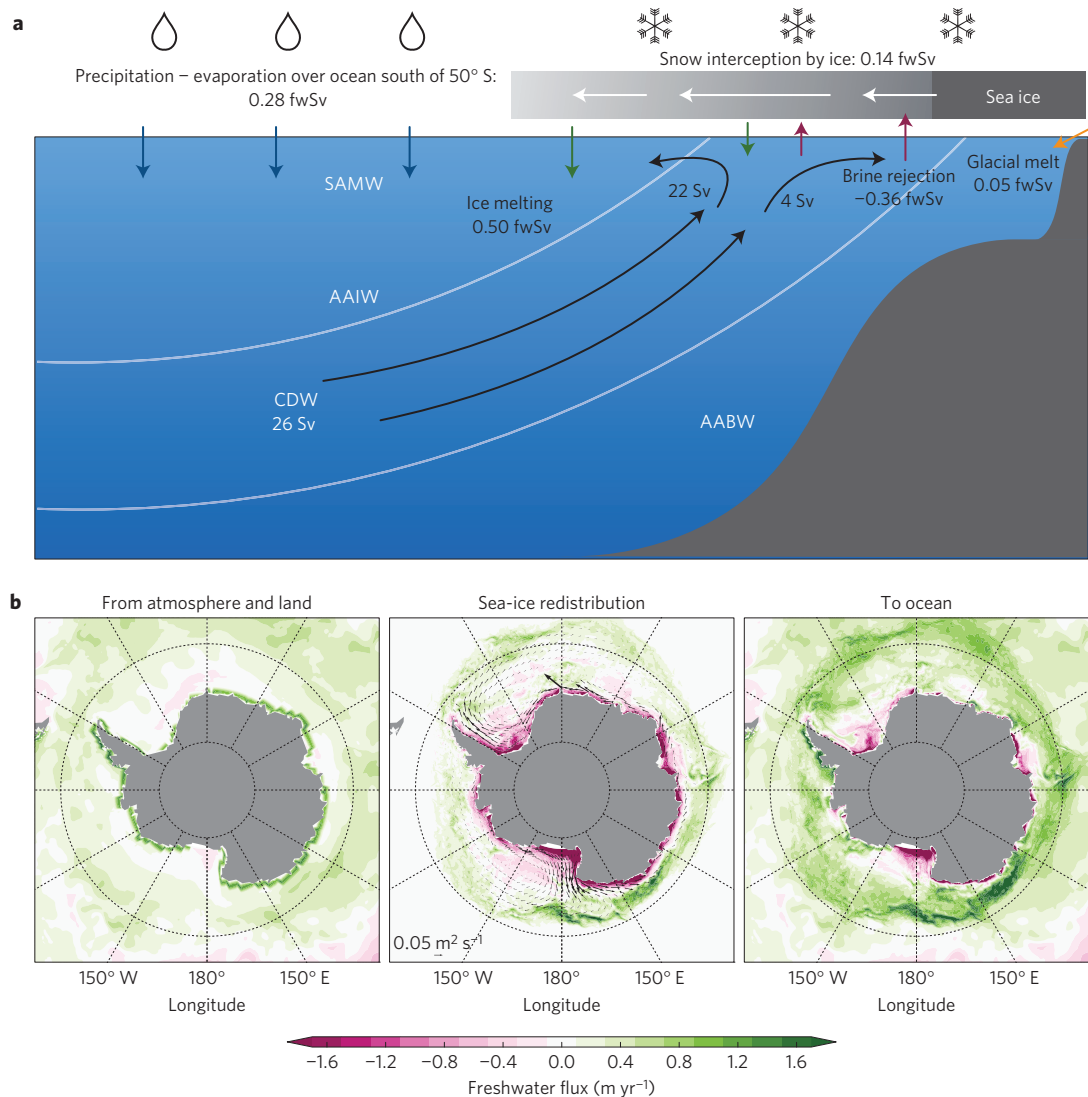


Figure 1 | Surface freshwater exchange in the SOSE. **a**, Schematic depicting the various bulk contributions to the freshwater exchange at the ocean surface south of 50° S (positive downward). Net fluxes are given in units of freshwater sverdrups¹¹: 1 fwSv = $10^6 \text{ m}^{-3} \text{ freshwater s}^{-1} \approx 3.15 \times 10^4 \text{ Gt freshwater per year}$. For reference, 1 fwSv ≈ 1.9 mm d⁻¹ of rainfall distributed over the region. **b**, Annual mean freshwater fluxes for the period 2005–2011. The left panel shows the flux leaving the atmosphere and land, and the right panel shows the flux entering the ocean. The centre panel shows the sea-ice redistribution flux (the difference between the two), with arrows indicating the lateral sea-ice thickness transport.

the thermodynamics of overturning. (Transformation rates are in sverdrups, 1 Sv = $10^6 \text{ m}^{-3} \text{ seawater s}^{-1}$.)

First we consider the overall transformation rate in the upper ocean in Fig. 2a (black), decomposed into the surface heat flux contribution (red), the surface freshwater flux contribution (blue), and interior mixing (dashed black). In agreement with other studies, surface freshwater fluxes dominate^{17,20}. The freshwater-driven transformation is characterized by a broad region of strongly negative transformation (that is, buoyancy gain) in the density range $26.6 < \gamma_n < 27.6 \text{ kg m}^{-3}$, peaking at more than 25 Sv, and a region of positive transformation (buoyancy loss) at higher densities ($\gamma_n > 27.6 \text{ kg m}^{-3}$). In Fig. 2b, the freshwater-flux transformation is decomposed into contributions from direct exchange with the atmosphere, land, and terrestrial ice (evaporation, precipitation and runoff/glacial ice melt; green), brine rejection from freezing sea ice (purple), and freshwater from melting ice (orange). Freezing and melting both contribute strongly, and in opposite senses (approximately ±20 Sv), to the transformation but do so over different density ranges. The positive peak in net freshwater-induced transformation near $\gamma_n = 27.7 \text{ kg m}^{-3}$ is caused by brine

rejection, while the transformation due to melting sea ice is larger than that due to precipitation. An alternative decomposition is to calculate the difference between the transformation that would have occurred if all of the precipitation passed directly to the ocean (dashed green) and the actual transformation (Fig. 2a, solid blue); this difference can be attributed to sea-ice freshwater redistribution (dashed blue), which is largely driven by the winds. The difference between the dashed and solid green lines reveals the effect of snow interception and transport by sea ice, which weakens transformation by up to 10 Sv in the Upper CDW (UCDW) range.

Upper-ocean mixing and mixed-layer entrainment also contribute significantly to water-mass transformation^{18,21}. As sea-ice growth, brine rejection and vertical mixing have a tightly coupled relationship in the Southern Ocean^{22,23}, mixing-induced transformation must be considered together with the surface fluxes. Figure 2c decomposes the mixing-induced transformation into contributions from vertical (solid) and horizontal/isopycnal (dashed) mixing of heat (red) and salinity (blue) in the upper 670 m (a depth that mostly encompasses the seasonal mixed layer; see Methods). Mixing is weaker overall than surface

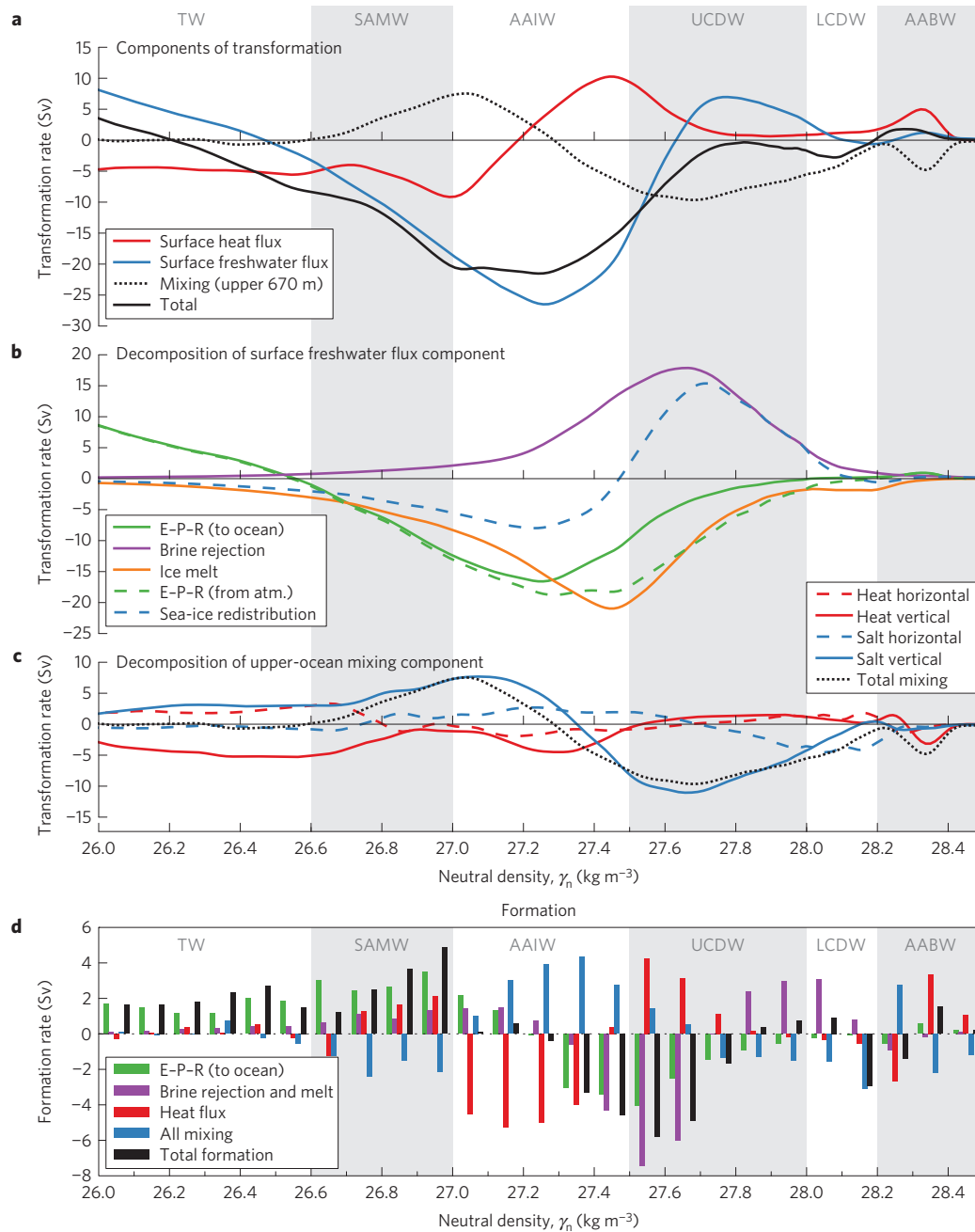


Figure 2 | Components of water-mass transformation and formation in SOSE in neutral density (γ_n) coordinates. The total transformation rate represents the net volume flux (in sverdrups, $1\text{ Sv} = 10^6 \text{ m}^3 \text{ s}^{-1}$) across an isopycnal surface. **a**, Total water-mass transformation (black) decomposed into contributions from surface heat flux (red), surface freshwater flux (blue), and upper-ocean mixing (dotted black). **b**, Decomposition of the surface-freshwater-flux-driven transformation into contributions from direct exchange with the atmosphere, land and terrestrial ice (evaporation, precipitation and runoff/glacial ice melt; green), brine rejection from freezing sea ice (purple), and freshwater from melting ice (orange); the three solid lines in **b** sum to give the blue line in **a**. An alternative decomposition of the freshwater-driven transformation into the sum of the potential transformation that would have occurred due to the atmospheric freshwater flux (dashed green) and the redistribution of freshwater by the sea ice (dashed blue). atm., atmosphere. **c**, Decomposition of mixing-induced transformation into contributions from vertical (solid) and horizontal/isopycnal (dashed) mixing of heat (red) and salt (blue) in the upper 670 m (a depth that encompasses most of the seasonal mixed layer). The black dotted line represents total mixing. **d**, Formation rates, summed in 0.1 kg m^{-3} neutral density bins, representing the convergence or divergence of water-mass transformation in the upper ocean. The total formation (black) is the sum of the coloured bars, which represent direct exchange with the atmosphere, land and terrestrial ice (evaporation, precipitation and runoff/glacial ice melt; green), sea-ice brine rejection and melt (purple), surface heat flux (red), and mixing (blue). The large-scale water masses are abbreviated as thermocline water (TW), Subantarctic Mode Water (SAMW), Antarctic Intermediate Water (AAIW), Upper Circumpolar Deep Water (UCDW), Lower Circumpolar Deep Water (LCDW), and Antarctic Bottom Water (AABW).

transformation. As in previous studies, vertical mixing of salinity is the dominant term¹⁷. The net mixing-induced transformation (black) is clearly homogenizing in nature, acting to densify water

of $\gamma_n < 27.5 \text{ kg m}^{-3}$ and lighten water above this value. The net upper-ocean transformation rate, comprising both surface fluxes and mixing, is shown in Fig. 2a as the solid black line. Downward

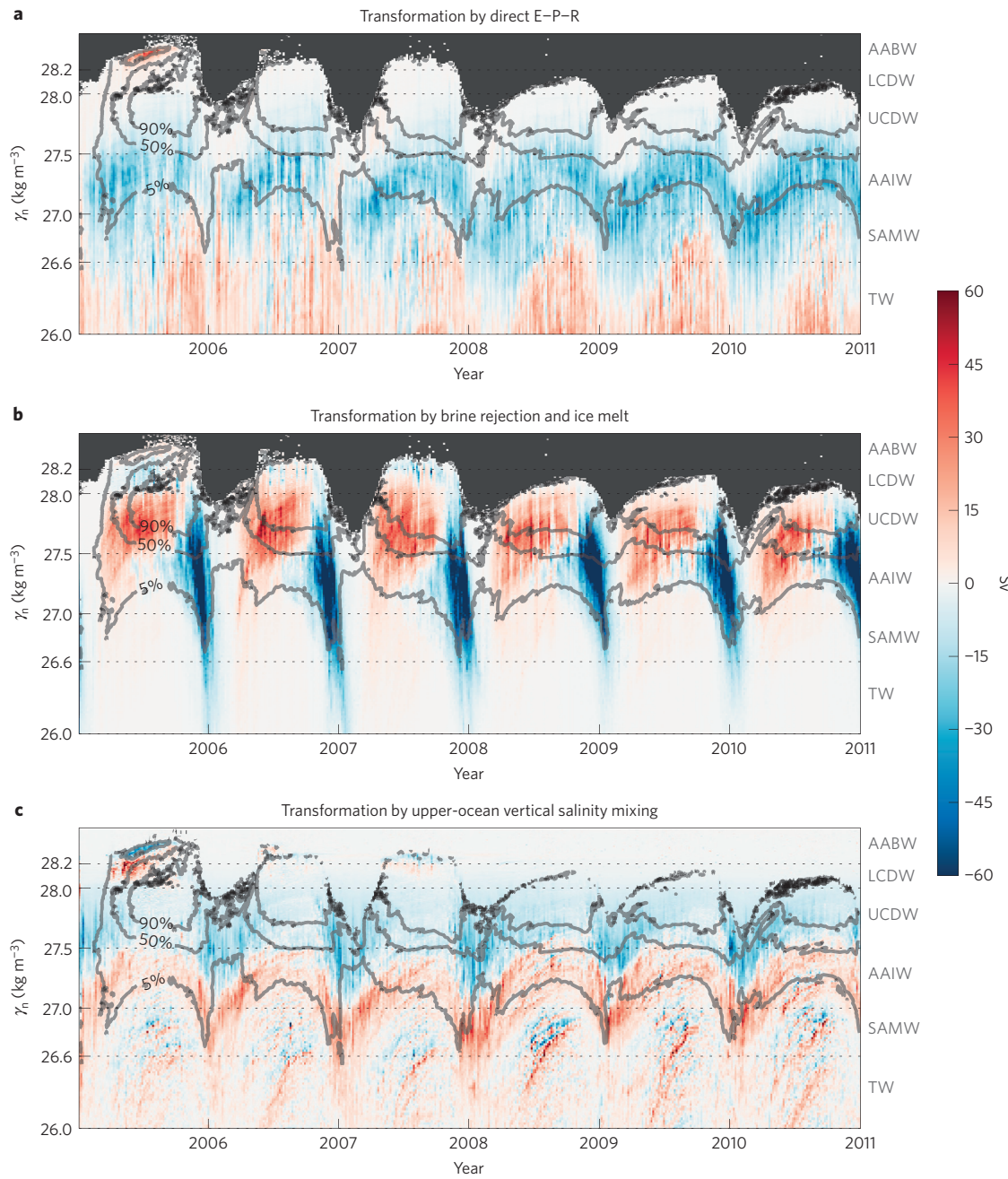


Figure 3 | Time series of freshwater transformation over the six-year state estimate, as a function of time (x axis) and neutral density γ_n (y axis).

a, Surface transformation due to direct freshwater exchange with the atmosphere (evaporation minus precipitation). The grey shaded area indicates isopycnals that outcrop neither under air nor ice, and the grey contours show the density-averaged sea-ice concentration (contours at 5%, 50% and 90%). **b**, Surface transformation due to ice freezing and melting. **c**, Transformation due to mixing of salinity in the upper 670 m.

mixing of freshwater from AAIW densities counteracts the positive transformation caused by surface fluxes (mostly brine rejection) in the UCDW range.

In Fig. 2d, we plot the formation rate, integrated in 0.1 kg m^{-3} density bins, for a select combination of components. The formation rate is the derivative of the transformation rate with respect to density. It represents the volume convergence in density space: negative formation (that is, destruction) in the upper ocean over a particular density range indicates that water in that range must be upwelled from the ocean interior. Examining first the net formation (black), we see a strong destruction of water in the range $27.3 < \gamma_n < 27.8 \text{ kg m}^{-3}$. Encompassing much of the UCDW densities and also denser AAIW, this clearly corresponds with the

upwelling branch of the meridional overturning circulation and the wind-driven Antarctic divergence. The combined effects of ice freezing and melt (purple) make the dominant contribution to this destruction, with precipitation (green) in second place. These processes are partially offset by heat fluxes (red) and mixing (blue), which instead drive formation in this range. At lower densities ($\gamma_n < 27.0 \text{ kg m}^{-3}$), strong formation is evident in the Subantarctic Mode Water (SAMW) range, driven by both heat and freshwater fluxes. In contrast with previous analysis that showed separate Indian and Pacific peaks in SAMW formation²⁴, the SAMW formation here is more broadly distributed due to interannual variability in the Indian and Pacific SAMW over the longer averaging period. At higher densities, heat fluxes drive

formation of AABW, with considerable opposition from vertical mixing. However, due to the lack of assimilated surface data for these densities, as well as the spurious nature of AABW production in SOSE, we consider the transformation and formation rates for $\gamma_n > 28.0 \text{ kg m}^{-3}$ unreliable; they are biased low compared with estimates from inverse modelling^{4,6,7}. (See Supplementary Information for model validation and related discussion.) In Supplementary Section 4, SOSE results are compared with a model with a better representation of AABW formation. Similar transformation rates for the lighter water masses lend confidence to our conclusions regarding the upper branch.

While the time-mean transformation rates presented above are what matter for net subduction and upwelling, examining the seasonal cycle in transformation provides insight into the physics of ice freezing and melt. In Fig. 3 we plot the temporal variability over the six-year SOSE period of the dominant freshwater transformation components: direct evaporation/precipitation/runoff/glacial ice melt (Fig. 3a), sea-ice freezing and melt (Fig. 3b), and the vertical mixing of salinity (Fig. 3c). This figure also shows sea-ice concentration averaged in density space, highlighting the relation between transformation and ice cover. The seasonal cycle in precipitation is clearly present but not particularly strong. In contrast, ice freezing and melt are extremely seasonal and correlated with the growth of ice cover. Particularly striking is the fact that melt fluxes reach far into the SAMW and thermocline density range²⁵. The mixing is also strongly seasonal, taking place mostly in summer and autumn. Together with the surface fluxes, the temporal variability is indicative of the creation of a shallow, fresh summer mixed layer following ice melt, which is subsequently eroded by vertical mixing through the autumn as ice reforms, consistent with simple models and under-ice observations^{22,23,26}. The intricate, temporally variable relationship between ice formation, freshwater fluxes, and mixing highlights the need for year-round observations to accurately quantify the net water-mass transformation driven by sea-ice processes.

Trends in sea-ice concentration have received much attention as a proxy for polar climate change²⁷. It has also been hypothesized that expanded Antarctic sea ice during the last glacial period was accompanied by a more vigorous AABW overturning circulation^{28,29}. From the ocean's perspective, however, it is sea-ice freshwater transport, rather than extent, that matters most. SOSE's short six-year time period does not permit us to examine the decadal trends in water-mass transformation directly; however, our results suggest that recent wind-driven trends in Antarctic sea-ice transport¹² should be associated with changes in water-mass transformation. It was recently proposed that these trends over the past 30 years, and the accompanying freshwater flux anomalies, can mostly explain decadal trends in Southern Ocean salinity (F. A. Haumann, N. Gruber, M. Muennich, I. Frenger and S. Kern., manuscript in preparation). Our transformation calculations imply that, if wind-driven sea-ice export increases, CDW will be converted into lighter water at a faster rate, potentially accelerating the upper limb of the overturning circulation.

Methods

Methods, including statements of data availability and any associated accession codes and references, are available in the online version of this paper.

Received 4 January 2016; accepted 27 May 2016;
published online 27 June 2016

References

1. Toggweiler, R. & Samuels, B. Effect of Drake Passage on the global thermohaline circulation. *Deep-Sea Res. I* **42**, 477–500 (1995).
2. Wolfe, C. & Cessi, P. The adiabatic pole-to-pole overturning circulation. *J. Phys. Oceanogr.* **41**, 1795–1810 (2011).
3. Nikurashin, M. & Vallis, G. A theory of the interhemispheric meridional overturning circulation and associated stratification. *J. Phys. Oceanogr.* **42**, 1652–1667 (2012).
4. Speer, K., Rintoul, S. & Sloyan, B. The diabatic Deacon cell. *J. Phys. Oceanogr.* **30**, 3212–3223 (2000).
5. Marshall, J. & Speer, K. Closing the meridional overturning circulation through Southern Ocean upwelling. *Nature Geosci.* **5**, 171–180 (2012).
6. Talley, L. D. Closure of the global overturning circulation through the Indian, Pacific and Southern Oceans: schematics and transports. *Oceanography* **26**, 80–97 (2013).
7. Jacobs, S. Bottom water production and its links with the thermohaline circulation. *Antarct. Sci.* **4**, 427–437 (2004).
8. Ren, L., Speer, K. & Chassignet, E. P. The mixed layer salinity budget and sea ice in the Southern Ocean. *J. Geophys. Res.* **116**, C08031 (2011).
9. Tamura, T., Ohshima, K. I., Nihashi, S. & Hasumi, H. Estimation of surface heat/salt fluxes associated with sea ice growth/melt in the Southern Ocean. *Sci. Online Lett. Atmos.* **7**, 17–20 (2011).
10. Walin, G. On the relation between sea-surface heat flow and thermal circulation in the ocean. *Tellus* **34**, 187–195 (1982).
11. Talley, L. D. Freshwater transport estimates and the global overturning circulation: shallow, deep and throughflow components. *Prog. Oceanogr.* **78**, 257–303 (2008).
12. Holland, P. R. & Kwok, R. Wind-driven trends in Antarctic sea-ice drift. *Nature Geosci.* **5**, 872–875 (2012).
13. Hasumi, H. & Sugino, N. Haline circulation induced by formation and melting of sea ice. *J. Geophys. Res.* **100**, 20613–20625 (1995).
14. Stoessel, A., Kim, S. & Drijfhout, S. B. The impact of Southern Ocean sea ice in a global ocean model. *J. Phys. Oceanogr.* **28**, 1999–2018 (1998).
15. Komuro, Y. & Hasumi, H. Effects of surface freshwater flux induced by sea ice transport on the global thermohaline circulation. *J. Geophys. Res.* **108**, 3047 (2003).
16. Saenko, O. A., Schmittner, A. & Weaver, A. J. On the role of wind-driven sea ice motion on ocean ventilation. *J. Phys. Oceanogr.* **32**, 3376–3395 (2002).
17. Iudicone, D., Madec, G., Blanke, B. & Speich, S. The role of Southern Ocean surface forcings and mixing in the global conveyor. *J. Phys. Oceanogr.* **38**, 1377–1400 (2008).
18. Marshall, J., Jamous, D. & Nilsson, J. Reconciling thermodynamic and dynamic methods of computation of water-mass transformation rates. *Deep-Sea Res. I* **46**, 545–572 (1999).
19. Urakawa, L. & Hasumi, H. Eddy-resolving model estimate of the cabbeling effect on the water mass transformation in the Southern Ocean. *J. Phys. Oceanogr.* **42**, 1288–1302 (2012).
20. Downes, S. M., Gnanadesikan, A., Griffies, S. M. & Sarmiento, J. L. Water mass exchange in the Southern Ocean in coupled climate models. *J. Phys. Oceanogr.* **41**, 1756–1771 (2011).
21. Garrett, C. & Tandon, A. The effects on water mass formation of surface mixed layer time-dependence and entrainment fluxes. *Deep-Sea Res. I* **44**, 1991–2006 (1997).
22. Gordon, A. L. & Huber, B. A. Southern Ocean winter mixed layer. *J. Geophys. Res.* **95**, 11544–11672 (1990).
23. Martinson, D. Evolution of the Southern Ocean winter mixed layer and sea ice: open ocean deepwater formation and ventilation. *J. Geophys. Res.* **95**, 11641–11654 (1990).
24. Cerovecki, I., Talley, L. D. & Mazloff, M. Subantarctic mode water formation, destruction, and export in the eddy-permitting Southern Ocean State Estimate. *J. Phys. Oceanogr.* **42**, 1485–1511 (2012).
25. Cerovecki, I. & Mazloff, M. R. The spatiotemporal structure of diabatic processes governing the evolution of Subantarctic Mode Water in the Southern Ocean. *J. Phys. Oceanogr.* **46**, 683–710 (2016).
26. Wong, A. P. S. & Riser, S. C. Profiling float observations of the upper ocean under sea ice off the Wilkes Land coast of Antarctica. *J. Phys. Oceanogr.* **41**, 1102–1115 (2011).
27. Cavalieri, D., Parkinson, C. & Vinnikov, K. Y. 30-year satellite record reveals contrasting Arctic and Antarctic decadal sea ice variability. *Geophys. Res. Lett.* **30**, 1970 (2003).
28. Stephens, B. B. & Keeling, R. F. The influence of Antarctic sea ice on glacial-interglacial CO₂ variations. *Nature* **404**, 171–174 (2000).
29. Ferrari, R. *et al.* Antarctic sea ice control on ocean circulation in present and glacial climates. *Proc. Natl Acad. Sci. USA* **111**, 8753–8758 (2014).

Acknowledgements

R.P.A. acknowledges support from NSF grant OCE-1357133. I.C., L.D.T. and M.M. acknowledge support from NSF grant OCE-1357072. L.D.T. and M.M. acknowledge additional support from NSF grant PLR-1425989, and M.M. from OCE-1234473. I.C. acknowledges additional support from the New International Fellowship Mobility Programme for Experienced Researchers—NEWFELPRO under the European Union's Seventh Framework Programme for research, technological

development and demonstration (FP7-PEOPLE-2011-COFUND-MCA). We acknowledge high-performance computing support from Yellowstone (ark:/85065/d7wd3xhc) provided by NCAR's Computational and Information Systems Laboratory, sponsored by the National Science Foundation, and from the Yeti HPC cluster, provided by Columbia University Research Computing Services. SOSE was produced with support from NSF-XSEDE grant OCE130007.

Author contributions

All authors contributed to the interpretation of the results and writing of the manuscript. R.P.A. designed the study, implemented the water-mass calculations, and conducted the validation against ship-based and sea-ice observations. I.C. contributed to the water-mass analysis and validation of SOSE against ARGO observations.

P.R.H. contributed to the analysis of sea-ice thermodynamics. E.N. contributed to the water-mass analysis. M.M. developed SOSE and contributed to model validation. L.D.T. contributed to interpretation of the transformation rates.

Additional information

Supplementary information is available in the [online version of the paper](#). Reprints and permissions information is available online at [www.nature.com/reprints](#). Correspondence and requests for materials should be addressed to R.P.A.

Competing financial interests

The authors declare no competing financial interests.

Methods

Southern Ocean State Estimate. Sparse observations are a major obstacle to accurate characterization of Southern Ocean physics. Current Antarctic sea-ice thickness and velocity measurements do not provide sufficient spatial and temporal resolution for an observationally derived sea-ice freshwater budget; nevertheless, there have been a few attempts to estimate the seasonal freshwater fluxes associated with sea-ice growth and melt from the limited observations^{8,9} (F. A. Haumann, N. Gruber, M. Muennich, I. Frenger and S. Kern., manuscript in preparation). All of these studies have shown that sea-ice-induced freshwater fluxes are large compared with typical precipitation rates. In addition to ice data, the water-mass transformation calculation further requires knowledge of the time-varying correlation between surface fluxes and the underlying water temperature and salinity. Given these challenges, our approach here is to use a highly realistic, carefully validated data-assimilating numerical model to examine the effects of sea-ice processes on Southern Ocean water masses.

Ocean state estimation is a form of data assimilation that provides an optimal synthesis of diverse observations consistent with known physical and thermodynamic constraints. It can be viewed as a logical extension of classical hydrographic inverse modelling³⁰. In its modern form, state estimation involves the use of a numerical general circulation model and its adjoint^{31,32}.

The Southern Ocean State Estimate³³ (SOSE) has been employed for numerous studies on topics including overturning circulation^{34,35}, air-sea fluxes³⁶, mode water formation^{24,25}, eddy mixing³⁷, and anthropogenic carbon transport³⁸. We employ SOSE iteration 100, a high-resolution general circulation model that has been constrained, via an adjoint method, to nearly all available observations, including sea-ice concentration, in the 2005–2010 period. This approach provides an optimal synthesis of the observations that is also consistent with known physical and thermodynamic constraints.

The numerical model underlying SOSE is the MITgcm^{39,40}. The model is configured on a 1/6° latitude-longitude grid with 42 unevenly spaced levels. This resolution is eddy permitting, and vigorous mesoscale motions are present in the solution. Mixed-layer physics are represented through the nonlocal K-profile parameterization scheme⁴¹. No mesoscale subgrid parameterization is used. The domain extends from the Antarctic coast to 24.6° S. SOSE is coupled to a viscous-plastic dynamic-thermodynamic sea-ice model⁴². Initial and open boundary conditions for SOSE temperature, salinity and velocity are taken from the Ocean Comprehensible Atlas global state estimate⁴³.

The adjoint method adjusts these initial and open boundary conditions, and the atmospheric variables that appear in the surface boundary conditions (collectively called the control variables), within their uncertainty range to minimize (in a least-squares sense) a cost function. The cost function is defined as the uncertainty-weighted misfit of the model state to the observations. Observational data sets include Argo profiles, Global Ocean Ship-based Hydrographic Investigations Program (GO-SHIP) data hydrographic data, Marine Mammals Exploring the Oceans Pole to Pole (MEOP) elephant-seal hydrographic data, infrared and microwave satellite sea-surface temperature, satellite-altimetry-derived sea-surface height, and several others³³. This adjustment process has been shown to reduce known biases in the NCEP (National Centers for Environmental Prediction) air-sea fluxes³⁶, lending confidence to the accuracy of the solution.

Optimization of the atmospheric state in SOSE was carried out in two stages. First, 2005–2007 was optimized, constrained to NCEP–NCAR (National Center for Atmospheric Research) reanalysis⁴⁴. Subsequently, 2008–2010 was optimized, using the more modern ERA-Interim reanalysis⁴⁵. For both simulations, fluxes of heat, freshwater and momentum were determined using a standard atmospheric boundary-layer scheme⁴⁶. SOSE does not include an ice-shelf model, and continental runoff/glacial ice melt was prescribed using a standard climatology⁴⁷. As precipitation is a control variable, it was possible for the optimization to change freshwater input near Antarctica, but inputs below the ocean surface, such as may be expected from ice-shelf influences, were not present. It was recently argued that subsurface glacial melt, while important for determining the salinity of AABW, does not make a large contribution to the open-ocean freshwater budget, which is our main focus here (F. A. Haumann, N. Gruber, M. Muennich, I. Frenger and S. Kern., manuscript in preparation). Nevertheless, the absence of subsurface glacial melt from SOSE is a serious limitation that may be addressed in future iterations.

SOSE was also constrained to sea-ice concentrations derived from passive microwave satellite radiometers. For the 2005–2007 optimization, concentrations were estimated using the ‘bootstrap’ algorithm⁴⁸. Due to lack of availability of this product when the 2008–2010 optimization began, for this period the concentrations were taken from the NASA-Team product^{49,50}. Descriptions of these products, including the satellite measurements they used, are available at <http://nsidc.org>. For both products, a spatially and temporally varying uncertainty of between 8.5 to 18% is prescribed⁵¹.

Comprehensive validation of SOSE sea ice and hydrography can be found in Supplementary Information. This validation indicates that SOSE hydrography agrees very well with observations in the SAMW, AAIW and UCDW range, which

are the primary focus of this study. The sea-ice model shows good agreement with remotely sensed sea-ice thickness and concentration data throughout the seasonal cycle. As with many numerical models⁵², SOSE does not properly represent the production of AABW ($\gamma_n > 28.2 \text{ kg m}^{-3}$) on the continental shelves. Although coastal polynyas, with high rates of sea-ice production, are present, HSSW is not formed at a significant rate. One possible reason is the treatment of glacial ice melt/runoff, which is applied at the surface right at the coast, rather than in subsurface ice cavities and broadly distributed iceberg melting. This freshwater source counteracts the brine rejection on the shelves in SOSE and prevents sufficient quantities of HSSW from forming. Another likely reason is the lack of sufficient resolution to represent boundary currents and cross-slope exchange, leading to biases in stratification and circulation^{53–55}. These shortcomings mean that we have low confidence in the SOSE estimate of transformation rates for Lower CDW (LCDW) and AABW ranges. In Supplementary Section 4, we compare the transformation rates from SOSE with a different model⁵⁶, which has a much better representation of shelf processes and HSSW production. The overall magnitude and structure of transformation, including the sea-ice components, are similar in both models, although the other model looks different in the LCDW and AABW ranges. This suggests that the representation of shelf processes in SOSE does not heavily bias our main conclusions regarding the role of sea ice in the upper branch of the Southern Ocean overturning.

Water-mass transformation. Transformation is calculated as

$$\Omega(\sigma, t) = \frac{\partial}{\partial \sigma} \int_{\sigma' < \sigma} \left(\frac{\partial \sigma}{\partial \theta} \dot{\theta} + \frac{\partial \sigma}{\partial S} \dot{S} \right) dV \quad (1)$$

where σ is potential density, t is time, and $\dot{\theta}$ and \dot{S} represent all non-advection sources (that is, external forcing and mixing) of potential temperature (θ) and salinity (S), respectively. The transformation rate Ω can be linearly decomposed into many different contributions from different processes, and the volume integral reduces to a surface integral for surface fluxes. Transformation was calculated ‘online’ within the model at every time step using the MITgcm LAYERS package. (Further technical details of the calculation are described in Supplementary Information.)

As this study is concerned with upper-ocean processes, we calculate transformation with respect to surface-referenced potential density (σ_θ); however, we interpolate potential density to neutral density (γ_n) when plotting to best identify well-known water masses. (See Supplementary Information for details of relabelling procedure.) We focus on the density range $\gamma_n > 26.0 \text{ kg m}^{-3}$. We define thermocline water (TW; $\gamma_n < 26.6 \text{ kg m}^{-3}$), Subantarctic Mode Water (SAMW; $26.6 < \gamma_n < 27.0 \text{ kg m}^{-3}$), Antarctic Intermediate Water (AAIW; $27.0 < \gamma_n < 27.5 \text{ kg m}^{-3}$), Upper Circumpolar Deep Water (UCDW; $27.5 < \gamma_n < 28.0 \text{ kg m}^{-3}$), Lower Circumpolar Deep Water (LCDW; $28.0 < \gamma_n < 28.2 \text{ kg m}^{-3}$) and Antarctic Bottom Water (AABW; $\gamma_n > 28.2 \text{ kg m}^{-3}$) following previous studies^{4,20}.

The specific choice of the upper 670 m for the integration volume of interior mixing terms was dictated by the depth of the discrete model grid cells. Sensitivity tests using integration depths ranging from 500 to 1,000 m showed that the results are not very sensitive to this choice.

Code availability. All code used to produce this study is public and freely available. The code used to produce SOSE, including the adjoint model, is part of the MITgcm framework and is available for download via <http://mitgcm.org>. The analysis was conducted using the open-source scientific Python software stack (<http://scipy.org>), and the analysis code is archived in a public Git repository https://bitbucket.org/ryanaberanthey/sose_water_mass_transformation.

Data availability. All data supporting the findings of this study are open and freely available. SOSE output can be downloaded at <http://sose.ucsd.edu>. Sea-ice thickness and concentration data (used for validation) are available from the National Snow and Ice Data Center: <http://nsidc.org>. GO-SHIP hydrographic data (used for validation) are available through the CLIVAR and Carbon Hydrographic Data Office website: <http://cchdo.ucsd.edu>. The Argo data were collected and made freely available by the International Argo Program and the national programmes that contribute to it (<http://www.argo.ucsd.edu>, <http://www.jcommops.org/argo>). The Argo Program is part of the Global Ocean Observing System.

References

30. Wunsch, C. Determining the general circulation of the oceans: a preliminary discussion. *Science* **196**, 871–875 (1977).
31. Wunsch, C. & Heimbach, P. in *Ocean Circulation and Climate: A 21st Century Perspective* Vol. 103 (eds Siedler, G., Gould, J. & Griffies, S. M.) Ch. 21, 553–579 (International Geophysics, Academic, 2013); <http://www.sciencedirect.com/science/article/pii/B9780123918512000210>

32. Forget, G. *et al.* ECCO version 4: an integrated framework for non-linear inverse modeling and global ocean state estimation. *Geosci. Model Dev. Discuss.* **8**, 3653–3743 (2015); <http://www.geosci-model-dev-discuss.net/8/3653/2015>
33. Mazloff, M., Heimbach, P. & Wunsch, C. An eddy permitting Southern Ocean state estimate. *J. Phys. Oceanogr.* **40**, 880–899 (2010).
34. Mazloff, M., Ferrari, R. & Schneider, T. The force balance of the Southern Ocean meridional overturning circulation. *J. Phys. Oceanogr.* **43**, 1193–1208 (2013).
35. Sebille, E. *et al.* Abyssal connections of Antarctic Bottom Water in a Southern Ocean state estimate. *Geophys. Res. Lett.* **40**, 2177–2182 (2013).
36. Cerovečki, I., Talley, L. D. & Mazloff, M. R. A comparison of Southern Ocean air-sea buoyancy flux from an ocean state estimate with five other products. *J. Clim.* **24**, 6283–6306 (2011).
37. Abernathey, R., Marshall, J., Shuckburgh, E. & Mazloff, M. Enhancement of mesoscale eddy stirring at steering levels in the Southern Ocean. *J. Phys. Oceanogr.* **40**, 170–185 (2010).
38. Ito, T., Woloszyn, M. & Mazloff, M. Anthropogenic carbon dioxide transport in the Southern Ocean driven by Ekman flow. *Nature* **463**, 80–83 (2010).
39. Marshall, J., Adcroft, A., Hill, C., Perelman, L. & Heisey, C. A finite-volume, incompressible Navier Stokes model for studies of the ocean on parallel computers. *J. Geophys. Res.* **102**, 5753–5766 (1997).
40. Marshall, J., Hill, C., Perelman, L. & Adcroft, A. Hydrostatic, quasi-hydrostatic, and nonhydrostatic ocean modeling. *J. Geophys. Res.* **102**, 5733–5752 (1997).
41. Large, W. G., McWilliams, J. C. & Doney, S. C. Oceanic vertical mixing: a review and a model with a nonlocal boundary layer parameterization. *Rev. Geophys.* **32**, 363–403 (1994).
42. Losch, M., Menemenlis, D., Campin, J., Heimbach, P. & Hill, C. On the formulation of sea-ice models. Part 1: effects of different solver implementations and parameterizations. *Ocean Modelling* **33**, 129–144 (2010).
43. Forget, G. Mapping ocean observations in a dynamical framework: a 2004–06 ocean atlas. *J. Phys. Oceanogr.* **40**, 1201–1221 (2010).
44. Kalnay, E. *et al.* The NCEP/NCAR 40-year reanalysis project. *Bull. Am. Meteorol. Soc.* **77**, 437–471 (1996).
45. Dee, D. *et al.* The ERA-Interim reanalysis: configuration and performance of the data assimilation system. *Q. J. R. Meteorol. Soc.* **137**, 553–597 (2011).
46. Large, W. G. & Yeager, S. G. The global climatology of an interannually varying air-sea flux data set. *Clim. Dynam.* **33**, 341–364 (2009).
47. Fekete, B. M., Vörösmarty, C. J. & Grabs, W. High-resolution fields of global runoff combining observed river discharge and simulated water balances. *Glob. Biogeochem. Cycles* **16**, 15-1–15-10 (2002).
48. Comiso, J. *Bootstrap Sea Ice Concentrations from Nimbus-7 SMMR and DMSP SSM/I-SSMIS version 2* (Technical Report, NASA DAAC at the National Snow and Ice Data Center, 2000).
49. Cavalieri, D., Parkinson, C., Gloersen, P. & Zwally, H. J. *Sea Ice Concentrations from Nimbus-7 SMMR and DMSP SSM/I-SSMIS Passive Microwave Data version 1* (Technical Report, NASA DAAC at the National Snow and Ice Data Center, 1996).
50. Markus, T. & Cavalieri, D. J. An enhancement of the NASA team sea ice algorithm. *IEEE Trans. Geosci. Remote Sens.* **38**, 1387–1398 (2000).
51. Fenty, I. G. & Heimbach, P. Coupled sea ice-ocean state estimation in the Labrador Sea and Baffin Bay. *J. Phys. Oceanogr.* **43**, 884–904 (2013).
52. Heuzé, C., Heywood, K. J., Stevens, D. P. & Ridley, J. K. Southern Ocean bottom water characteristics in CMIP5 models. *Geophys. Res. Lett.* **40**, 1409–1414 (2013).
53. Toggweiler, J. R. & Samuels, B. Effect of sea ice on the salinity of Antarctic bottom waters. *J. Phys. Oceanogr.* **25**, 1980–1997 (1995).
54. Stewart, A. L. & Thompson, A. F. Connecting Antarctic cross-slope exchange with Southern Ocean overturning. *J. Phys. Oceanogr.* **43**, 1453–1471 (2013).
55. Heywood, K. J. *et al.* Ocean processes at the Antarctic continental slope. *Phil. Trans. R. Soc. A* **372**, 20130047 (2014).
56. Holland, P. R. *et al.* Modeled trends in Antarctic sea ice thickness. *J. Clim.* **27**, 3784–3801 (2014).